On the relationship between molecular hydrogen and carbon monoxide abundances in molecular clouds

S. C. O. Glover[1]★ and M.-M. Mac Low[2]★

[1]*Zentrum für Astronomie der Universität Heidelberg, Institut für Theoretische Astrophysik, Albert-Ueberle-Str. 2, 69120 Heidelberg, Germany*
[2]*Department of Astrophysics, American Museum of Natural History, Central Park West at 79th Street, New York, NY 10024, USA*

ABSTRACT

The most usual tracer of molecular gas is line emission from CO. However, the reliability of this tracer has long been questioned in environments different from the Milky Way. We study the relationship between H_2 and CO abundances using a fully dynamical model of magnetized turbulence coupled to a chemical network simplified to follow only the dominant pathways for H_2 and CO formation and destruction, and including photodissociation using a six-ray approximation. We find that the abundance of H_2 is primarily determined by the amount of time available for its formation, which is proportional to the product of the density and the metallicity, but insensitive to photodissociation. Photodissociation only becomes important at extinctions under a few tenths of a visual magnitude, in agreement with both observational and prior theoretical work. On the other hand, CO forms quickly, within a dynamical time, but its abundance depends primarily on photodissociation, with only a weak secondary dependence on H_2 abundance. As a result, there is a sharp cut-off in CO abundance at mean visual extinctions $A_V \lesssim 3$. At lower values of A_V, we find that the ratio of H_2 column density to CO emissivity $X_{CO} \propto A_V^{-3.5}$. This explains the discrepancy observed in low metallicity systems between cloud masses derived from CO observations and other techniques such as infrared emission. Our work predicts that CO-bright clouds in low metallicity systems should be systematically larger or denser than Milky Way clouds, or both. Our results further explain the narrow range of observed molecular cloud column densities as a threshold effect, without requiring the assumption of virial equilibrium.

Key words: molecular processes – ISM: clouds – ISM: molecules – galaxies: ISM.

1 INTRODUCTION

Observed star formation takes place within giant molecular clouds (GMCs), so understanding how these clouds form and evolve is a key step towards understanding star formation on galactic scales. The main chemical constituent of any GMC is molecular hydrogen (H_2). However, it is extremely difficult to directly observe this molecular hydrogen *in situ*. Radiative transitions in H_2 are weak, owing to the molecule's lack of a permanent dipole moment. Moreover, the lowest lying rotational energy levels of H_2 are widely spaced, and so are very rarely excited in gas with the temperatures typical of GMCs, $T \sim 10$–20 K. For this reason it is common to use emission from carbon monoxide (CO), the second-most abundant molecule in GMCs, as a proxy for the H_2.

In order to use CO as a proxy for H_2, however, it is necessary to understand the relationship between the distributions of these two molecules. Both are readily dissociated by the absorption of ultra-violet (UV) photons with energies below the Lyman limit of atomic hydrogen, so in low density, low extinction gas such as the warm neutral component of the interstellar medium (ISM), the abundances of both molecules will be small. However, the two molecules form rather differently: H_2 forms predominantly on the surface of dust grains (Gould & Salpeter 1963), while CO forms almost exclusively in the gas phase, via any one of a number of chains of ion–neutral or neutral–neutral reactions [see e.g. Sternberg & Dalgarno (1995) for a useful summary of CO formation chemistry]. Moreover, H_2 can protect itself from UV radiation via self-shielding, which becomes effective for relatively low H_2 column densities (Draine & Bertoldi 1996). The corresponding process for CO is less effective (Lee et al. 1996), requiring a higher column density, and the low abundance of carbon relative to hydrogen in the ISM means that the required column density typically corresponds to a situation in which a large fraction of the available carbon is already locked up in the form of CO. For these reasons, we would expect the CO/H_2 ratio to vary through a cloud, and this expectation is confirmed by detailed models of slab-like or spherical clouds (e.g. Röllig

★E-mail: sglover@ita.uni-heidelberg.de (SCOG); mordecai@amnh.org (M-MML)

et al. 2007). These find that the transition from atomic hydrogen to molecular hydrogen occurs at a point closer to the cloud surface than the transition from ionized carbon, via neutral atomic carbon, to CO.

Although spatial variations in the CO/H_2 ratio within a GMC would appear to make it difficult to use CO as a proxy for H_2, observations of Galactic GMCs show that in fact there appears to be a good correlation between the integrated intensity of the $J = 1 \rightarrow 0$ rotational transition line of ^{12}CO and the H_2 column density (see e.g. Dickman 1978; Sanders, Solomon & Scoville 1984; Solomon et al. 1987; Strong & Mattox 1996; Dame, Hartmann & Thaddeus 2001). A number of independent studies have shown that GMCs in the Galactic disc all have CO-to-H_2 conversion factors that are approximately

$$X_{CO} = \frac{N_{H_2}}{W_{CO}} \simeq 2 \times 10^{20} \text{ cm}^{-2} \text{ K}^{-1} \text{ km}^{-1} \text{ s}, \qquad (1)$$

where W_{CO} is the velocity-integrated intensity of the CO $J = 1 \rightarrow 0$ emission line, averaged over the projected area of the GMC, and N_{H_2} is the mean H_2 column density of the GMC, averaged over the same area. Although the former can be directly observed, the latter cannot. However, for nearby clouds, it can be inferred from measurements of the diffuse γ-ray flux produced by interactions between high energy cosmic rays and atomic hydrogen, atomic helium and H_2. The γ-ray flux along a given line of sight depends on the total hydrogen column density along that line of sight. Since the atomic hydrogen column density can be measured via its 21-cm emission, the H_2 column density can be inferred. As the values for X_{CO} obtained in this way are consistent with those obtained by assuming that the GMCs are in virial equilibrium and using the observed linewidth–size relation to compute the cloud mass (e.g. Solomon et al. 1987), it is generally accepted that CO emission is indeed a good proxy for H_2 mass in nearby GMCs.

However, the issue of the environmental dependence of X_{CO} remains highly contentious. In gas with a lower metallicity, or a higher ambient UV radiation field, CO photodissociation will be more effective, and the amount of CO in the cloud will be smaller, with the CO-rich gas occupying a smaller volume than in the Galactic case (e.g. Maloney & Black 1988, Molina et al., in preparation). The mean H_2 abundance may also be smaller, but the greater role played by H_2 self-shielding means that we do not expect the H_2 abundance to be nearly as sensitive to changes in the metallicity. Because of this, there are good theoretical reasons to expect the relationship between CO emission and H_2 mass to change as we change the metallicity. However, observational efforts to test this yield inconsistent results.

Measurements of X_{CO} that assume that extragalactic GMCs are in virial equilibrium and use a virial analysis to determine the cloud mass generally find values for X_{CO} that are similar to those obtained in the Milky Way, with at most a weak metallicity dependence (Wilson 1995; Rosolowsky et al. 2003; Bolatto et al. 2008). On the other hand, measurements that constrain GMC masses using other techniques that do not depend on the CO emission, such as by measuring the far-infrared dust emission, consistently find values for X_{CO} that are much larger than the Galactic value and that are suggestive of a strong metallicity dependence (Israel 1997; Rubio et al. 2004; Leroy et al. 2007, 2009).

Numerical simulations provide us with one way to address this observational dichotomy. If we can understand the distribution of CO and H_2 in realistic models of GMCs, then we may begin to understand why the different types of observation give such different

results. However, until very recently, the ability of simulations to address this issue has been quite limited. Sophisticated treatments of gas and grain chemistry, radiative heating and cooling, and radiative transfer have been developed to model GMCs [see, for instance, the paper by Röllig et al. (2007) which compares results from a number of popular codes], but the very complexity of these models limits their applicability to highly simplified geometries: typically the adopted cloud models are one-dimensional, assuming either spherical symmetry (e.g. Stoerzer; Stutzki & Sternberg 1996) or a semi-infinite, uniform slab (e.g. Le Petit et al. 2006).

Moreover, the modelling often assumes that the chemistry of the clouds is in equilibrium, which is valid only if all of the chemical time-scales are much shorter than any dynamical time-scale associated with the GMCs. Since real GMCs are observed to be highly inhomogeneous, and to be dominated by supersonic turbulent motions (see e.g. Mac Low & Klessen 2004, and references therein), the applicability of the results from these simple spherical or slab models to real clouds is open to question. On the other hand, previous attempts to accurately model the turbulent dynamics of GMCs and the inhomogeneous and intermittent density structure that is created by this turbulence typically have avoided modelling the cloud chemistry, rendering them also of limited use in addressing this question. The few studies that have attempted to model both the turbulence and the chemistry self-consistently (e.g. Joulain et al. 1998; Lesaffre, Gerin & Hennebelle 2007; Godard, Falgarone & Pineau des Fôrets 2009) have typically done so by reducing the dimensionality of the problem. For instance, Godard et al. (2009) present results on the chemical evolution of gas passing through magnetized, turbulent vortices, using two-dimensional simulations of these vortices, and then construct models for lines of sight through diffuse clouds by summing up the contributions from a number of different vortices. However, it is unclear whether the results obtained in this fashion are the same as those that would be obtained using a fully three-dimensional model for the turbulence.

In a previous paper (Glover et al. 2010, hereafter Paper I), we presented the first results from a project that aimed to combine detailed chemical modelling with three-dimensional magnetohydrodynamical turbulence simulations in order to self-consistently model both the chemistry and the turbulent dynamics of the gas within a GMC. We showed that it is now computationally feasible to attempt this. Provided one makes a few simplifying assumptions regarding the extent of the chemistry to be treated, and the treatment of the UV radiation field, it is possible to model both the H_2 and the CO chemistry of a GMC with acceptable accuracy within a moderate resolution dynamical simulation. Paper I presented results from a few trial simulations performed using only one set of cloud properties (mean density, metallicity, etc.). In this paper, we present results from a much larger set of simulations that examine the sensitivity of H_2 and CO formation to changes in the mean densities and metallicities of GMCs, and explore the consequences of this for the CO-to-H_2 conversion factor and the dynamical structure of the observed clouds.

In Section 2, we discuss our numerical approach and the initial conditions used for our simulations. In Section 3, we present the main results of our simulations and use them to derive the approximate dependence of the CO-to-H_2 conversion factor on cloud properties. In Section 4, we discuss the major consequences of our findings. In Section 5, we discuss a few potential caveats regarding our approach and show why they are unlikely to significantly affect our main results. Finally, in Section 6, we close with a brief summary.

2 SIMULATIONS

2.1 Numerical method

Our simulations were performed using a modified version of the ZEUS-MP magnetohydrodynamical code (Norman 2000; Hayes et al. 2006) fully described in Paper I. Our modifications include the addition of a simplified treatment of hydrogen, carbon and oxygen chemistry, composed of 218 reactions between 32 chemical species, together with a detailed atomic and molecular cooling function. This treatment includes the formation of H_2 on the surface of dust grains, following a prescription taken from Hollenbach & McKee (1979). The formation rate of H_2 per unit volume due to grain surface reactions is written as

$$R_{H_2} = \gamma_{H_2} \left(\frac{Z}{Z_\odot} \right) n n_H \, \mathrm{cm}^{-3} \, \mathrm{s}^{-1}, \tag{2}$$

where n is the number density of hydrogen nuclei, n_H is the number density of atomic hydrogen, Z is the metallicity of the gas and γ_{H_2} is the rate coefficient for H_2 formation, given by

$$\gamma_{H_2} = \frac{3.0 \times 10^{-17} T_2^{1/2} f_a}{1.0 + 0.4(T_2 + T_{d,2})^{1/2} + 0.2 T_2 + 0.08 T_2^2}, \tag{3}$$

where $T_2 = T/100 \, \mathrm{K}$ is the gas temperature in units of 100 K, $T_{d,2} = T_d/100 \, \mathrm{K}$ is the dust temperature in units of 100 K and where

$$f_a = \frac{1}{1 + 10^4 \exp{(-600/T_d)}}. \tag{4}$$

For simplicity, we fix the dust temperature at 10 K in all of the simulations presented in this paper. Aside from this reaction, we include no other grain surface chemistry in our current models.

We model the photodissociation of H_2 using prescriptions for dust shielding and H_2 self-shielding taken from Draine & Bertoldi (1996). For CO photodissociation, we account for dust shielding, CO self-shielding and shielding by H_2, using shielding functions taken from Lee et al. (1996) for the last two terms. To compute the column densities of dust, H_2 and CO required by this treatment of photodissociation, we use the six-ray approximation introduced in Glover & Mac Low (2007a). In this approximation, we compute photochemical rates in each zone in our simulation volume by averaging over the six lines of sight that lie parallel to the coordinate axes.

2.2 Initial conditions

All of our simulations begin with an initially uniform gas distribution, with mean hydrogen nucleus number density n_0. The initial temperature of the gas is 60 K. However, because the cooling time of the gas is significantly shorter than the dynamical time in all but our lowest density runs, the gas temperature quickly adjusts itself until the gas is close to thermal equilibrium, and hence our results are largely insensitive to our choice for the initial temperature. The initial velocity field is turbulent, with uniform power between wavenumbers $k = 1$ and 2 and with an initial rms velocity of $5 \, \mathrm{km \, s^{-1}}$. We drive the turbulence so as to maintain approximately the same rms velocity throughout the simulation, following the method described in Mac Low et al. (1998) and Mac Low (1999).

We assume that the gas is magnetized, with an initially uniform magnetic field strength $B_0 = 5.85 \, \mu\mathrm{G}$ and a field that is initially oriented parallel to the z-axis of the simulation. In Glover & Mac Low (2007b) we showed that the time-scale for H_2 formation in

a turbulent, magnetized cloud is relatively insensitive to the value chosen for the magnetic field strength, and hence we do not expect our results to be particularly sensitive to our choice of B_0. The particular value that we have chosen is the same as we adopted in Paper I and is motivated by the 21-cm observations by Heiles & Troland (2005) that find a median magnetic field strength of ∼6 μG for the cold neutral medium.

We assume that the gas has a uniform metallicity Z and that the initial fractional abundances (by number) of carbon and oxygen relative to hydrogen are given by $x_{C^+} = x_{C,tot} = 1.41 \times 10^{-4} (Z/Z_\odot)$ and $x_O = x_{O,tot} = 3.16 \times 10^{-4} (Z/Z_\odot)$, where $x_{C,tot}$ and $x_{O,tot}$, respectively, refer to carbon and oxygen in all forms (ionized, neutral, or incorporated into molecules). For solar metallicity, this corresponds to the values given in Sembach et al. (2000). As in Glover & Mac Low (2007b), we ignore the effects of metals other than C or O, in order to minimize the computational requirements of our simulations. We assume a standard dust-to-gas ratio for our solar metallicity runs and also assume that in our lower metallicity runs, the dust-to-gas ratio scales linearly with metallicity. We assume that the dust has an extinction curve characterized by $R_V = 3.1$ and that this is independent of metallicity. We also fix the dust temperature at 10 K in every run.

We adopt a fixed cosmic ray ionization rate $\zeta = 10^{-17} \, \mathrm{s}^{-1}$. For the majority of our simulations, we use the same spectral shape and normalization for the interstellar radiation field as in Draine (1978). For brevity, when we refer to the strength of the radiation field in a simulation, we typically give it in terms of G_0, the ratio of the field strength relative to the strength of the Draine field. Thus, in the majority of our simulations, $G_0 = 1.0$. We also performed a few simulations without a radiation background, i.e. with $G_0 = 0.0$. The effects of increasing G_0 to much larger values are examined in a separate paper (Glover et al., in preparation).

We perform our simulations in a cubical volume of side L to which we apply periodic boundary conditions. As we have previously noted in Paper I, the use of periodic boundary conditions for the gas together with what are effectively non-periodic boundary conditions for the radiation is not self-consistent, and we adopt this arrangement purely for the computational convenience that it offers. We do not include the effects of self-gravity in our current simulations but intend to explore them in future work.

We have performed simulations with a range of different initial densities n_0 and metallicities Z, as detailed in Table 1. For most of these simulations, we set $L = 20 \, \mathrm{pc}$, but we have also performed a few simulations with $L = 5 \, \mathrm{pc}$. For all of these simulations, we adopt a numerical resolution of 128^3 zones, which we showed in Paper I was sufficient to yield converged results for the mass-weighted mean abundances of CO and H_2, at least to the level of accuracy required here.

We evolved all of our runs until $t_{end} = 1.8 \times 10^{14} \, \mathrm{s} \simeq 5.7 \, \mathrm{Myr}$, corresponding to roughly three eddy turnover times for the turbulence. In Paper I, we showed that this gave sufficient time for the density distribution, temperature distribution and the chemical abundance of CO all to reach a statistical steady state. We expect the same to be true for the majority of runs examined here. However, as we will see later, there is evidence that the CO abundance in some of our lowest density runs has not reached a steady state by $t = t_{end}$. Therefore, in four of our lowest density runs (runs n30, n100, n30-Z01 and n100-Z01), we did not stop at this point but continued to evolve them until a time $t_{ext} = 7.2 \times 10^{14} \, \mathrm{s} \simeq 22.8 \, \mathrm{Myr}$. We note, however, that it is questionable whether real molecular clouds could live for so long without undergoing localized

Table 1. List of simulations.

ID	n_0 (cm^{-3})	Z (Z$_\odot$)	Box size (pc)	G_0
n30	30	1.0	20	1.0
n100	100	1.0	20	1.0
n180	180	1.0	20	1.0
n300	300	1.0	20	1.0
n1000	1000	1.0	20	1.0
n300-Z06	300	0.6	20	1.0
n100-Z03	100	0.3	20	1.0
n300-Z03	300	0.3	20	1.0
n30-Z01	30	0.1	20	1.0
n100-Z01	100	0.1	20	1.0
n300-Z01	300	0.1	20	1.0
n1000-Z01	1000	0.1	20	1.0
n1000-Z003	1000	0.03	20	1.0
n30-L5	30	1.0	5	1.0
n100-L5	100	1.0	5	1.0
n300-L5	300	1.0	5	1.0
n1000-L5	1000	1.0	5	1.0
n30-UV0	30	1.0	20	0.0
n100-UV0	100	1.0	20	0.0
n300-UV0	300	1.0	20	0.0
n1000-UV0	1000	1.0	20	0.0

Note. G_0 is the UV field strength in units of the Draine (1978) field.

gravitational collapse and forming stars, physics that is not included in our current models.

3 RESULTS

3.1 Density and temperature structure of the gas

Before considering the molecular abundances produced in the various simulations, it is perhaps useful to briefly discuss the density and temperature distributions generated by the turbulence. As an illustrative example, we plot in Fig. 1(a) the mass-weighted density probability distribution function (PDF) for runs n300 and n30. The PDFs are plotted in terms of the dimensionless logarithmic density contrast $s \equiv \ln(\rho/\rho_0)$, where ρ_0 is the mean density of the gas. It is clear from the plot that the two PDFs have a similar form when plotted in dimensionless units. Both PDFs are roughly lognormal, with similar widths and means, as expected from previous studies of supersonic turbulence in interstellar gas (Padoan, Nordlund & Jones 1997). Deviations from the lognormal form are apparent in the wings of the PDFs, where one would expect the effects of turbulent intermittency to be most pronounced (Kritsuk et al. 2007; Schmidt et al. 2009; Federrath et al. 2010).

It is also interesting to compare the temperature PDFs of the same two runs (Fig. 1b). If we do so, we find that the gas is systematically warmer in run n30 than in run n300, owing to the increased effectiveness of photoelectric heating and reduced effectiveness of CO cooling in the lower density run. We find similar behaviour in our other runs, and so for reasons of brevity, we will not plot their density and temperature PDFs here. In each case, we find a roughly lognormal density PDF, as expected, with a width that is correlated with the mean temperature of the gas. Reducing the density and/or the metallicity of the gas tends to increase its mean temperature, both by reducing the efficiency of cooling and by increasing the influence of photoelectric heating, and hence the lower density and lower metallicity runs have narrower density PDFs than the higher density or higher metallicity runs. This trend is also apparent if one
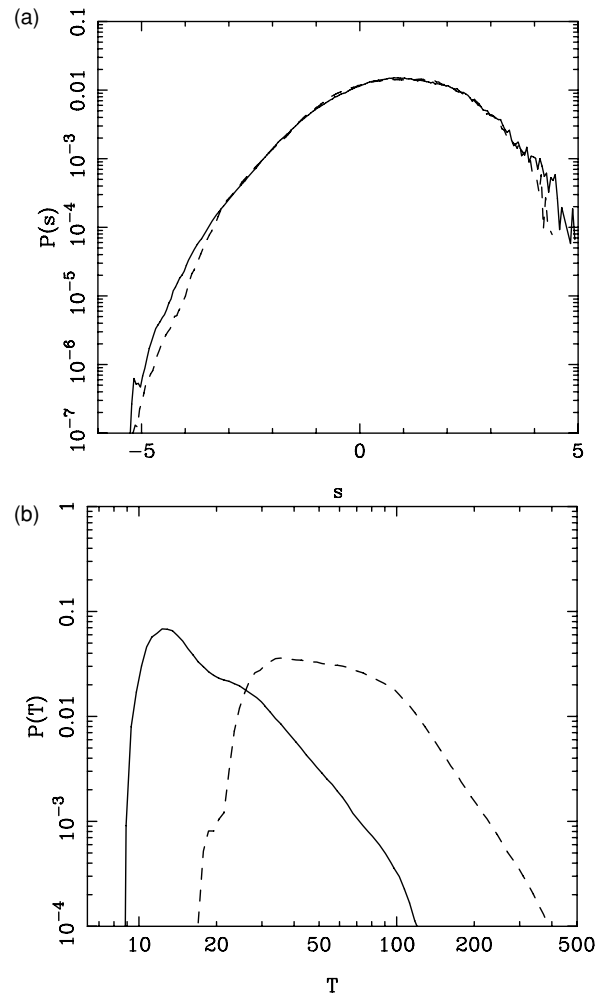

Figure 1. (a) Mass-weighted PDF of the logarithmic density contrast $s = \ln(\rho/\rho_0)$, where ρ_0 is the mean density of the gas, plotted for runs n300 (solid line) and n30 (dashed line). Both of the PDFs display the lognormal shape characteristic of quasi-isothermal supersonic turbulence. (b) Mass-weighted temperature PDF for runs n300 (solid line) and n30 (dashed line). The characteristic temperature of the gas in run n30 is much higher than in run n300, owing to a combination of the effects of the lower gas density and the low CO abundance (see Section 3.2), which render cooling much less effective, and the lower level of dust extinction, which significantly increases the importance of photoelectric heating. Note that while the relatively sharp cut-off in the PDF for run n30 at $T < 30$ K appears to be real, the corresponding feature at $T < 10$ K in the PDF for run n300 is not; the latter is a consequence of the fact that for technical reasons, our cooling function cuts off at $T = 10$ K (see Paper I).

looks at the clumping factor of the gas, defined as

$$C = \frac{\langle \rho^2 \rangle}{\langle \rho \rangle^2}, \qquad (5)$$

which ranges from $C \simeq 4.5$ in run n1000-Z003 to $C \simeq 6.8$ in run n1000, with the values from the other runs spread fairly evenly between these two extremes. These values are consistent with those inferred from models of some Galactic photodissociation regions (e.g. Kramer et al. 2004, whose results imply a mean value for C of roughly 5 in W3 Main), although other regions show evidence for much higher values of C (e.g. Falgarone & Phillips 1996).

Although these results are not particularly surprising given our findings in Glover & Mac Low (2007b) and in Paper I, they do

serve to demonstrate that the density structure produced by the turbulence is rather different from the structure that is often assumed in models of clumpy photodissociation regions (PDR). These models commonly assume that the density structure of a PDR can be represented by a population of clumps (usually assumed to be spherical, but with densities and sizes that can vary from clump to clump), embedded in some much lower density interclump medium (see e.g. Burton; Hollenbach & Tielens 1990; Meixner & Tielens 1993; Spaans & van Dishoeck 1997; Mookerjea et al. 2006). However, the density distributions generated by the turbulence in our simulations do not fit comfortably into this picture. The fact that we find density PDFs that are smooth, single-peaked functions without even a hint of bimodal behaviour suggests that any attempt to partition the gas into high density clumps embedded in a much lower density medium will inevitably wind up being somewhat arbitrary, since there is no particular density or range of densities that one can pick out of the PDF as corresponding to a 'clump', and hence no obvious way to determine where a 'clump' ends and the interclump gas begins. This unfortunately makes it difficult to compare our results with those coming from these clumpy PDR models, but also does serve to emphasize the great importance of modelling the dynamics and chemistry of the gas in a self-consistent fashion.

3.2 Molecular abundances: dependence on extinction and gas density

Let us now turn our attention from the density and temperature of the gas to its chemical content. In Table 2, we list the mass-weighted mean abundances of H_2 and CO, denoted $\langle x_{H_2}\rangle_M$ and $\langle x_{CO}\rangle_M$ respectively, at our default end-point $t = t_{end} = 5.7$ Myr, for each of the simulations that we have run. These mean abundances are defined as

$$\langle x_{H_2}\rangle_M = \frac{2}{M}\Delta V \sum_{i,j,k} \frac{n_{H_2}(i,j,k)}{n(i,j,k)}\rho(i,j,k) \qquad (6)$$

Table 2. Mass-weighted mean abundances of H_2 and CO at our default stopping time, $t = t_{end}$.

ID	$\langle x_{H_2}\rangle_M$	$\langle x_{CO}\rangle_M$
n30	0.351	9.31(−9)
n100	0.689	2.97(−6)
n180	0.847	1.92(−5)
n300	0.943	6.41(−5)
n1000	0.998	1.27(−4)
n300-Z06	0.874	2.10(−5)
n100-Z03	0.357	2.19(−8)
n300-Z03	0.712	2.74(−6)
n30-Z01	0.027	2.27(−12)
n100-Z01	0.136	8.27(−11)
n300-Z01	0.385	1.66(−7)
n1000-Z01	0.816	2.32(−6)
n1000-Z003	0.449	6.08(−8)
n30-L5	0.342	3.80(−10)
n100-L5	0.817	1.26(−8)
n300-L5	0.982	9.00(−6)
n1000-L5	0.998	8.17(−5)
n30-UV0	0.345	1.84(−5)
n100-UV0	0.687	8.39(−5)
n300-UV0	0.944	1.39(−4)
n1000-UV0	0.998	1.41(−4)

and

$$\langle x_{CO}\rangle_M = \frac{1}{M}\Delta V \sum_{i,j,k} \frac{n_{CO}(i,j,k)}{n(i,j,k)}\rho(i,j,k), \qquad (7)$$

respectively, where M is the total mass in the simulation, ΔV is the volume of a single grid zone, $n(i,j,k)$ is the number density of hydrogen nuclei in zone (i,j,k), $n_{H_2}(i,j,k)$ and $n_{CO}(i,j,k)$ are the H_2 and CO number densities in the same zone, $\rho(i,j,k)$ is the mass density in that zone, and where we sum over all grid zones. Note that the inclusion of the factor of 2 in our definition of $\langle x_{H_2}\rangle_M$ is to ensure that when the hydrogen is fully molecular, we will have $\langle x_{H_2}\rangle_M = 1.0$, rather than 0.5, as this will hopefully be less confusing for the reader.

In Fig. 2(a), we plot the values of $\langle x_{H_2}\rangle_M$ at $t = t_{end}$ as a function of the mean visual extinction, $\langle A_V\rangle$, and in Fig. 2(b), we give a similar plot of the values of $\langle x_{CO}\rangle_M$ at $t = t_{end}$. The mean visual extinction $\langle A_V\rangle$ is defined as

$$\langle A_V\rangle = \frac{1}{N^2}\sum_{j,k} A_{V,j,k}, \qquad (8)$$

where N is the number of grid zones along one edge of the box, $A_{V,j,k}$ is the visual extinction along the line of sight running parallel to the x-axis and with y and z coordinates (j,k), and where we sum over all sets of (j,k) corresponding to zone centres. Note that our choice to project along the x-axis is arbitrary and that projecting along the y- or z-axis would yield the same value of $\langle A_V\rangle$, which indeed is simply given by

$$\langle A_V\rangle = f_{conv}n_0 L, \qquad (9)$$

where f_{conv} is the conversion factor between the column density of H nuclei and the visual extinction. This is given by $f_{conv} = 5.348 \times 10^{-22}(Z/Z_\odot)$ mag cm^2 for our choice of dust properties.

To understand these results, first consider only the runs performed with our default values for L and G_0. Fig. 2(a) shows that if we disregard the $L = 5$ pc runs, then a clear correlation exists between $\langle x_{H_2}\rangle_M$ and $\langle A_V\rangle$, with larger values of $\langle A_V\rangle$ yielding larger values of $\langle x_{H_2}\rangle_M$. Similarly, if we disregard the $G_0 = 0.0$ runs, then Fig. 2(b) shows that there is also a clear, and far stronger, correlation between $\langle x_{CO}\rangle_M$ and $\langle A_V\rangle$. If we compare the runs with $\langle A_V\rangle = 1$ and $\langle A_V\rangle = 10$, then we see a factor of 2–3 change in $\langle x_{H_2}\rangle_M$, compared with a change in $\langle x_{CO}\rangle_M$ of 3–4 orders of magnitude. Plotting $\langle x_{H_2}\rangle_M$ and $\langle x_{CO}\rangle_M$ against the mean gas number density n_0 shows no clear correlation in either case (Fig. 3), if we consider the data as a whole, but also shows that both $\langle x_{H_2}\rangle_M$ and $\langle x_{CO}\rangle_M$ correlate well with density at fixed metallicity and with metallicity at fixed density.

At first glance, these results suggest that both the H_2 and the CO abundances are controlled by photodissociation, with the CO responding far more strongly to changes in $\langle A_V\rangle$ than the H_2. However, the results of the $L = 5$ pc runs challenge this interpretation. They lie where we would expect in the plot of $\langle x_{CO}\rangle_M$ versus $\langle A_V\rangle$ (Fig. 2b), but they lie to the left of the corresponding $L = 20$ pc runs in the plot of $\langle x_{H_2}\rangle_M$ versus $\langle A_V\rangle$ (Fig. 2a). Indeed, shifting them uniformly to the right by a factor of 4 brings them into good agreement with the other runs. This result can be understood if we realize that the real correlation responsible for the behaviour seen in Fig. 2(a) is not that between $\langle x_{H_2}\rangle_M$ and $\langle A_V\rangle$, but is instead a correlation between $\langle x_{H_2}\rangle_M$ and $n_0 Z$. Since $\langle A_V\rangle \propto n_0 Z$, we find an apparent correlation between $\langle x_{H_2}\rangle_M$ and $\langle A_V\rangle$ if we compare only runs with the same box size L. However, if we change L without changing $n_0 Z$, we will still obtain the same value of $\langle x_{H_2}\rangle_M$ but find that it now corresponds to a different mean visual extinction.

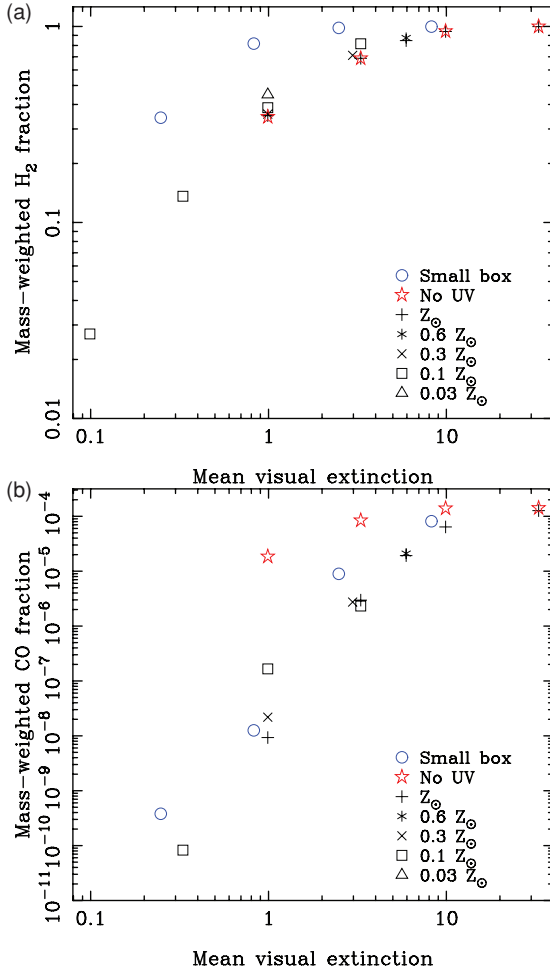**Figure 2.** (a) Mass-weighted mean H_2 fraction, plotted as a function of the mean visual extinction $\langle A_V \rangle$. Different symbols are used for runs with different metallicities, box sizes or UV field strengths, as outlined in the legend. The runs performed using an $L = 5$ pc box (blue circles) produce as much H_2 as the corresponding $L = 20$pc runs (crosses), and so the former are simply displaced to the left of the latter by a factor of 4. This fact, together with the fact that the runs performed without a UV background (red stars) follow the same apparent correlation as the runs with a UV background, provides convincing evidence that the apparent correlation between $\langle x_{H_2} \rangle_M$ and $\langle A_V \rangle$ is artificial: the true correlation is between $\langle x_{H_2} \rangle_M$ and $n_0 Z$, and the apparent correlation with $\langle A_V \rangle$ arises because $\langle A_V \rangle \propto n_0 Z L$. (b) As (a), but for the mean mass-weighted CO fraction. In this case, the $L = 5$pc runs show the same correlation between the mean CO fraction and the mean extinction as the $L = 20$ pc runs, but the runs performed without a UV background do not. This suggests that the correlation between $\langle x_{CO} \rangle_M$ and $\langle A_V \rangle$ is real.

This result strongly suggests that the differences in the mean H_2 abundance found at the end of the different runs are not a result of photodissociation and that this plays little or no role in regulating the amount of H_2 present in the gas. Instead, the dependence of $\langle x_{H_2} \rangle_M$ on $n_0 Z$ suggests that the amount of H_2 present depends simply on the H_2 formation time, t_{form,H_2}, which scales as $t_{form,H_2} \propto 1/(n_0 Z)$. If $n_0 Z$ is small, then the H_2 formation time is long, and the hydrogen in the gas simply does not have sufficient time to become fully molecular by the end of the simulation, despite the boost to the H_2 formation rate resulting from the presence of the turbulent compressions. On the other hand, when $n_0 Z$ is large, the hydrogen can easily become almost fully molecular.
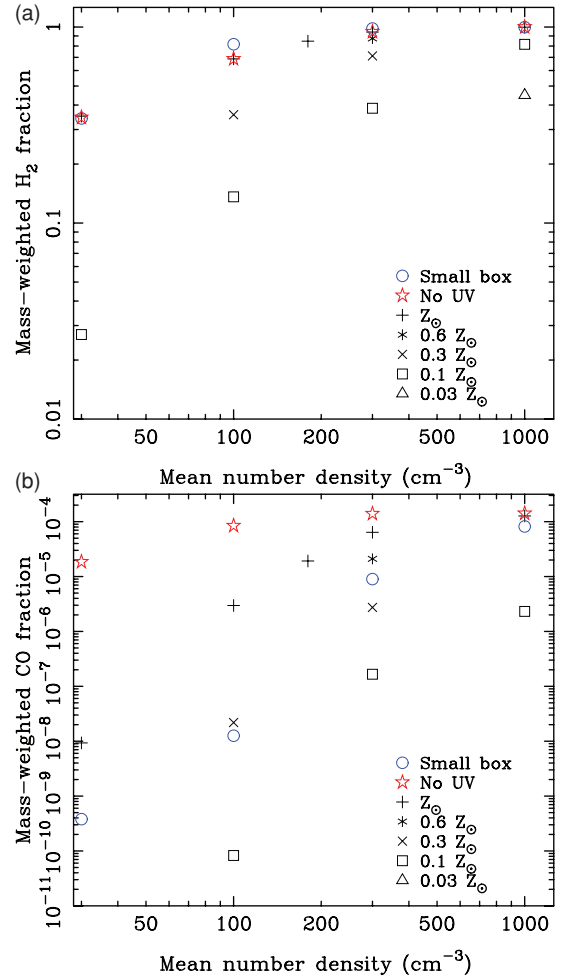
Figure 3. (a) Mass-weighted mean H_2 fraction, plotted as a function of mean density n_0. We see a clear dependence on density at fixed metallicity and a clear dependence on metallicity at fixed density, consistent with $\langle x_{H_2} \rangle_M$ correlating with the product of density and metallicity. (b) As (a), but for the mean mass-weighted CO fraction. Again, the CO fraction depends on density at fixed metallicity and depends on metallicity at fixed density, but now the CO fraction also depends strongly on the box size L. Density by itself, without knowledge of L or Z, predicts the CO fraction poorly.

In contrast, the CO abundances in these runs respond in the fashion that we would expect them to if they were primarily controlled by photodissociation. Decreasing L while holding $n_0 Z$ constant leads to a sharp drop in the CO abundance, implying that in this case the correlation with $\langle A_V \rangle$ is real and not simply a consequence of the relationship between $n_0 Z$ and $\langle A_V \rangle$.

We can confirm this interpretation by considering what happens in the runs that are performed with $G_0 = 0.0$ to eliminate all photodissociation. We see from Fig. 2(a) that in this case, we still recover the same correlation between $\langle x_{H_2} \rangle_M$ and $\langle A_V \rangle$. However, in the absence of an UV background, the H_2 abundance *cannot* depend on the visual extinction, as the only physical processes in the simulation that depend on the visual extinction are those involving the attenuation of the UV background. Therefore, the correlation between $\langle x_{H_2} \rangle_M$ and $\langle A_V \rangle$ cannot be real and must simply be a consequence of the actual correlation between $\langle x_{H_2} \rangle_M$ and $n_0 Z$, or rather the inverse correlation between $\langle x_{H_2} \rangle_M$ and the mean H_2 formation time. On the other hand, Fig. 2(b) shows that the CO abundance at low $\langle A_V \rangle$ is much larger in the runs without a UV

background, consistent with a picture in which the CO abundance is primarily controlled by photodissociation.

Fig. 2(b) also demonstrates that the CO abundance is not determined solely by photodissociation, since even in the absence of the UV background, we see a systematic decrease in the CO abundance as we move to lower densities. This decrease is driven primarily by the decrease in the mean H$_2$ abundance, since H$_2$ is a key component in most of the chemical pathways capable of forming gas-phase CO. We have verified this by running simulations similar to runs n30-UV0 and n100-UV0 that start with all of the hydrogen in molecular form. The CO abundances produced in these runs are significantly higher than in the runs that start with atomic hydrogen: in the lower density run, roughly 60 per cent of the available carbon is converted to CO, while in the higher density run, roughly 95 per cent is converted. In comparison, the fraction of carbon converted to CO in runs n30-UV0 and n100-UV0 is 13 and 60 per cent, respectively. Nevertheless, it is clear from Fig. 2(b) that the dependence of the CO abundance on the H$_2$ abundance is a relatively small effect in comparison with the dependence of the CO abundance on the mean visual extinction in the runs with a UV background: the former is responsible for changes in $\langle x_{CO} \rangle_M$ of a factor of a few, while the latter is responsible for changes of several orders of magnitude.

We have thus arrived at the first key result of this paper: in a turbulent molecular cloud, the mean H$_2$ abundance depends primarily on the time taken to form the H$_2$ and is insensitive to photodissociation, while the CO abundance is determined primarily by photodissociation, with only a secondary dependence on the H$_2$ fraction.

3.3 Molecular abundances: time dependence

We can get further confirmation of the results of the previous section by considering the time dependence of $\langle x_{H_2} \rangle_M$ and $\langle x_{CO} \rangle_M$. In Fig. 4, we plot the evolution of these quantities as a function of time for a set of runs with different mean densities at solar metallicity, while in Fig. 5, we show a similar plot for runs with a metallicity $Z = 0.1 \, Z_\odot$. Looking at the evolution of H$_2$ fraction with time in these figures, we see that the time required to convert a large fraction of the initial atomic hydrogen to molecular hydrogen decreases as we increase the density or the metallicity, just as we would expect given the results of the previous section. Moreover, it is clear that in most of the runs, the mean H$_2$ fraction has yet to reach equilibrium at the end of the run. Finally, extrapolation of the curves beyond 6 Myr suggests that the H$_2$ fraction in all of the runs should eventually reach a value of order unity; there is no indication that the equilibrium value of $\langle x_{H_2} \rangle_M$ will be significantly smaller than 1 in any of the runs.

The time evolution of $\langle x_{CO} \rangle_M$ in the different runs is qualitatively different from that of $\langle x_{H_2} \rangle_M$. CO forms rapidly at the beginning of the simulations, but after roughly a million years, the rate of increase of the CO abundance slows or stops. The amount of CO formed during this initial period of rapid evolution depends strongly on the mean visual extinction of the gas, with the runs with low $\langle A_V \rangle$ forming considerably less CO than the runs with high $\langle A_V \rangle$. The subsequent evolution of the CO abundance depends on the value of $\langle x_{H_2} \rangle_M$ at this point. If $\langle x_{H_2} \rangle_M \sim 1$, as in run n300 or n1000, then there is little further evolution of the CO abundance. On the other hand, if the mean H$_2$ abundance remains significantly smaller than unity at this early point, then the CO abundance continues to increase, driven by the increasing availability of H$_2$, and may double or triple by the end of the run.

It is also evident that $\langle x_{CO} \rangle_M$ displays far larger fluctuations in runs with low mean visual extinctions (e.g. run n30 or n100-Z01)

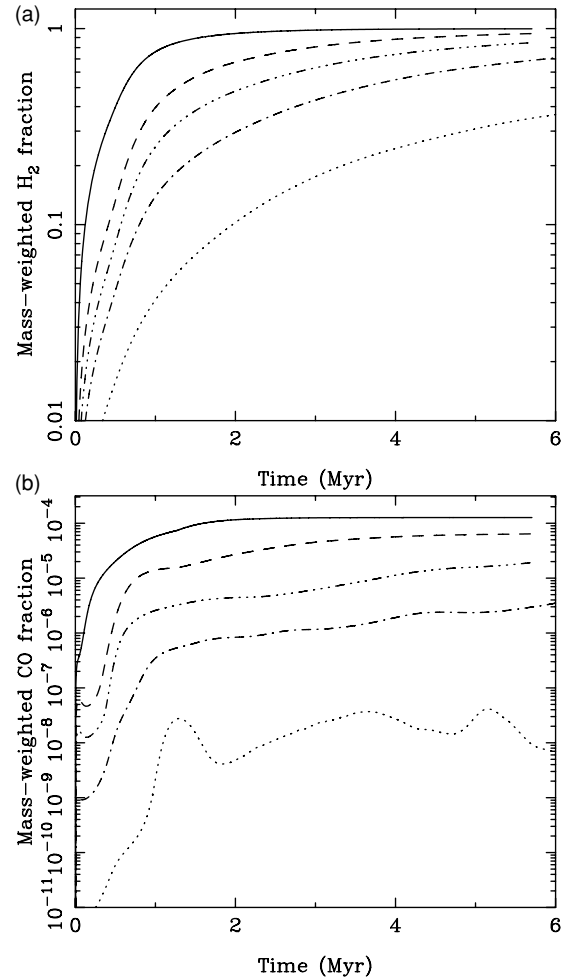**Figure 4.** (a) Evolution of the mass-weighted mean H$_2$ abundance with time in runs n1000 (solid line), n300 (dashed line), n180 (dash–dot–dot–dotted line), n100 (dash–dotted line) and n30 (dotted line). (b) As (a), but for the mass-weighted mean CO abundance. The large fluctuations seen in run n30 occur because the dominant contribution to $\langle x_{CO} \rangle_M$ in this simulation comes from only a few transient CO-rich clumps. As the turbulence forms and destroys them, their contribution to $\langle x_{CO} \rangle_M$ undergoes large fluctuations. In the higher density runs, many more structures contribute significantly to $\langle x_{CO} \rangle_M$ and so the influence of the formation or destruction of any one clump is much smaller.

than in runs with high mean visual extinctions. This is a consequence of the difference in the spatial distribution of the CO in a low extinction run compared to a high extinction run. When $\langle A_V \rangle$ is small, the CO fraction in most of the gas is very small, owing to the lack of effective shielding of the CO against UV photodissociation. In this case, most of the CO in the simulation is found in a small number of dense, comparatively well-shielded clumps. Since our simulations were performed without self-gravity, these clumps are transient objects and are continually being disrupted and reformed by the turbulence. This continual variation in the number and nature of the CO-rich clumps leads to the observed variation in the mass-weighted mean CO abundance. On the other hand, when $\langle A_V \rangle$ is large, far more of the gas has a high CO fraction, and many more clumps and other dense structures such as sheets and filaments contribute to $\langle x_{CO} \rangle_M$. Although all of these structures are transient, just as in the low $\langle A_V \rangle$ runs, the fact that a much larger number of structures contribute to $\langle x_{CO} \rangle_M$ than in the low $\langle A_V \rangle$ runs means that
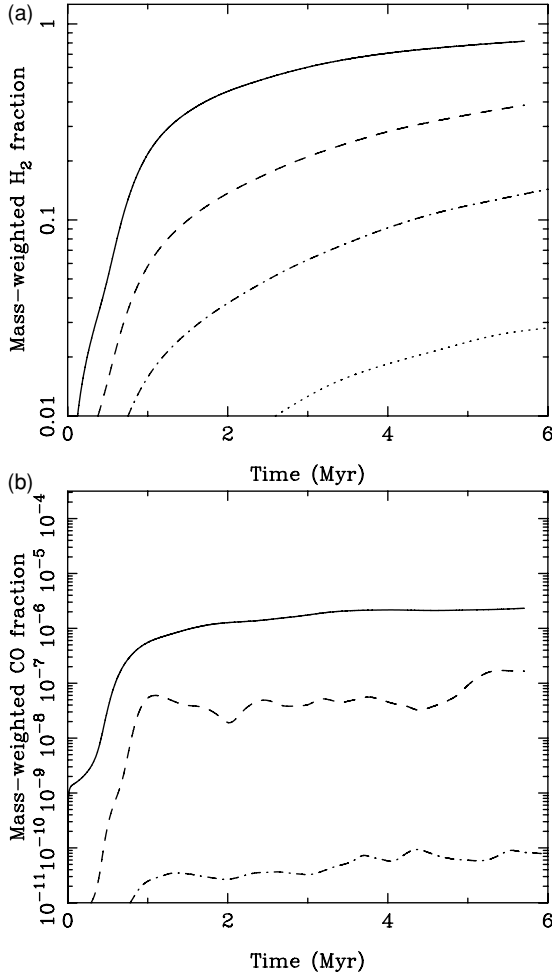
Figure 5. (a) Evolution of the mass-weighted mean H_2 abundance with time in runs n1000-Z01 (solid line), n300-Z01 (dashed line), n100-Z01 (dash–dotted line) and n30-Z01 (dotted line). (b) Evolution of the mass-weighted mean CO abundance with time in runs n1000-Z01 (solid line), n300-Z01 (dashed line) and n100-Z01 (dash–dotted line). In run n30-Z01, the mean CO abundance remains smaller than 10^{-11} for the whole period plotted. Reducing the metallicity clearly has a much more pronounced effect on the CO than on the H_2.

the variation in $\langle x_{CO} \rangle_M$ resulting from the creation or destruction of any particular clump or filament is much smaller.

In Fig. 6, we show how $\langle x_{H_2} \rangle_M$ and $\langle x_{CO} \rangle_M$ vary with time in runs n30-UV0, n100-UV0, n300-UV0 and n1000-UV0, all performed without a UV background. The evolution of the H_2 fraction in these runs is very similar to that in the runs with a UV background, again showing that photodissociation plays little or no role in regulating the growth of the H_2 abundance. On the other hand, the evolution of the CO abundance in these runs is clearly different from that in the runs with a UV background. The increase in the CO abundance in these runs more clearly tracks the increase in the H_2 abundance, and there is no longer any significant feature at $t \sim 1$ Myr (other than in run n1000-UV0, which has converted almost all of its carbon into CO by this point). The CO abundances produced in the lower density runs are also clearly much larger than in the corresponding runs with a UV background, and there is no indication that they have yet reached equilibrium.

Finally, in Fig. 7, we plot the time evolution of $\langle x_{H_2} \rangle_M$ and $\langle x_{CO} \rangle_M$ in the four runs that we evolved for a much longer time. The values
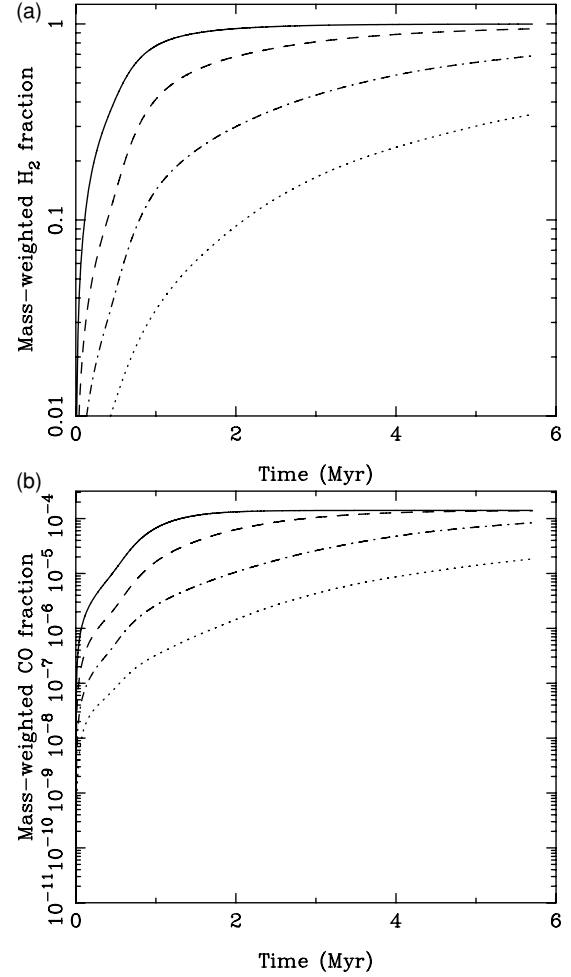
Figure 6. (a) Evolution of the mass-weighted mean H_2 abundance with time in runs n1000-UV0 (solid line), n300-UV0 (dashed line), n100-UV0 (dash–dotted line) and n30-UV0 (dotted line). (b) As (a), but for the mass-weighted mean CO abundance.

of $\langle x_{H_2} \rangle_M$ and $\langle x_{CO} \rangle_M$ at the end of these runs are listed in Table 3. Figure 7 further emphasizes that time is the primary factor controlling the H_2 abundance in the runs in which the product $n_0 Z$ is small. For instance, at $t \sim 5$ Myr, the mass-weighted mean H_2 fraction in run n100-Z01 is only 10 per cent, but it has increased to roughly 40 per cent by $t \sim 20$ Myr, i.e. it has increased almost linearly with time. The only one of these runs in which H_2 photodissociation appears to play an important role is run n30-Z01, in which the mean H_2 fraction appears to saturate at roughly 5 per cent. The mean visual extinction of the gas in this run is only 0.1 mag, while in run n100-Z01, which is not significantly affected by the UV, it is approximately 0.3 mag, suggesting that the critical value below which UV photodissociation begins to significantly limit the H_2 abundance lies somewhere in the range $\langle A_V \rangle \sim 0.1$–0.3. This corresponds to a mean column density of hydrogen nuclei of $\langle N_H \rangle \sim 2$–$6 \times 10^{20}$ cm^{-2}, which compares well with the finding by the *Copernicus* satellite that there is a sudden jump in the H_2 abundance along galactic sightlines with $\log N_H > 20.7$, consistent with the onset of self-shielding (Savage et al. 1977). It also agrees within a factor of a few with the critical extinction $A_{V,crit} \simeq 0.5$ derived by Krumholz, McKee & Tumlinson (2008) for idealized spherical clouds.
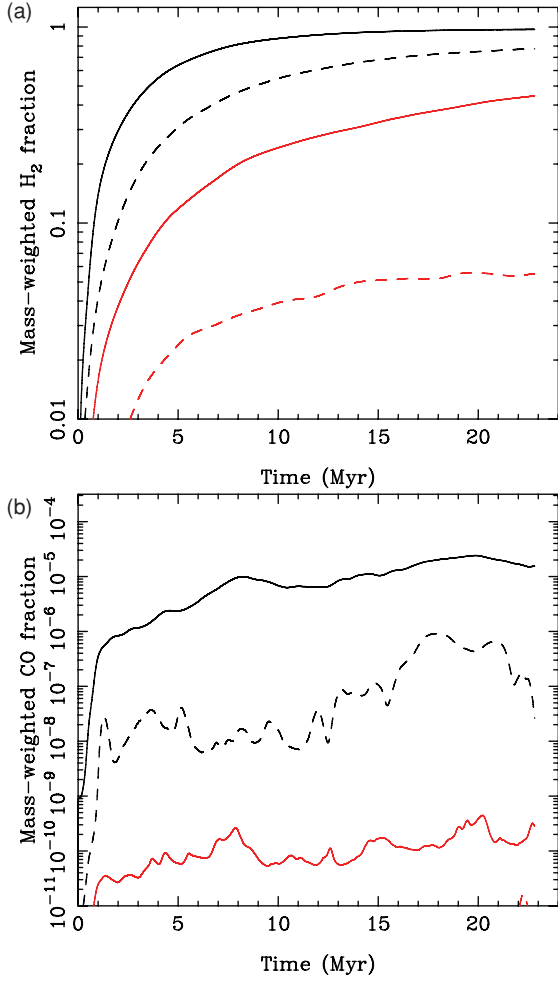
(a)

(b)

Figure 7. (a) Evolution of the mass-weighted mean H_2 abundance with time in runs n100 (black solid line), n30 (black dashed line), n100-Z01 (red solid line) and n30-Z01 (red dashed line). (b) As (a), but for the mass-weighted mean CO abundance. Note that in run n30-Z01, the mean CO abundance remains smaller than 10^{-11} for almost the whole of the period plotted, becoming barely visible in the plot only after $t \sim 22\,\mathrm{Myr}$.

Table 3. Mass-weighted mean abundances of H_2 and CO at the end of our extended runs.

ID	$\langle x_{H_2} \rangle_M$ at t_{ext}	$\langle x_{CO} \rangle_M$ at t_{ext}
n30	0.774	2.63(−8)
n100	0.972	1.55(−5)
n30-Z01	0.055	6.78(−12)
n100-Z01	0.445	2.84(−10)

3.4 Estimating the CO-to-H₂ conversion factor

It is of particular interest to understand how the distinct chemical changes we see as we decrease $\langle A_V \rangle$ affect the CO-to-H_2 conversion factor, X_{CO}. The decrease of $\langle x_{CO} \rangle_M$ by almost 4 orders of magnitude between $\langle A_V \rangle = 10$ and 1 is suggestive of a strong correlation between X_{CO} and $\langle A_V \rangle$, but does not by itself allow us to quantify the relationship between these two quantities. The sharp decrease in $\langle x_{CO} \rangle_M$ as we decrease $\langle A_V \rangle$ is reflected in a sharp decrease in the column density of CO along most sightlines, as illustrated in Fig. 8.
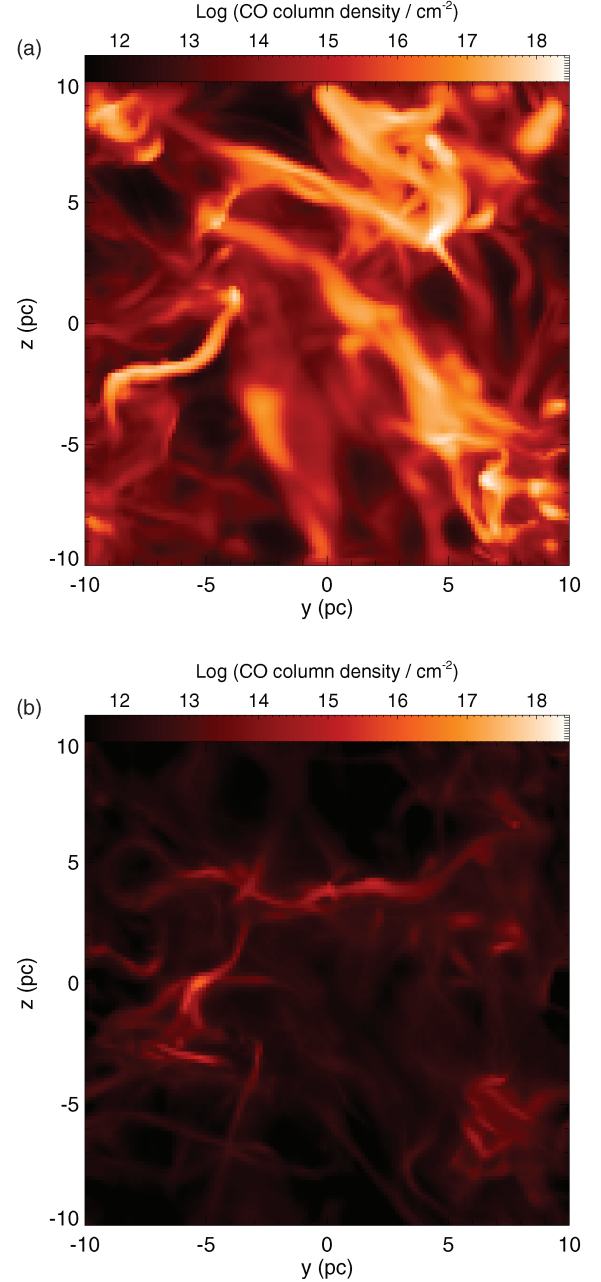
(a)

(b)

Figure 8. (a) CO column density in run n100 at time $t = t_{end}$, viewed along a line of sight parallel to the x-axis of the simulation. (b) As (a), but for run n30. The contrast with run n100 is striking and illustrates how a relatively small change in the mean extinction can produce a large change in the appearance of the cloud.

This also suggests a strong correlation between X_{CO} and $\langle A_V \rangle$, but still does not allow us to make a quantitative statement.

To quantify the relationship between X_{CO} and $\langle A_V \rangle$, we need to be able to at least approximately compute

$$X_{CO} \equiv \frac{N_{H_2}}{W_{CO}}, \qquad (10)$$

where W_{CO} is the velocity-integrated intensity of the $J = 1 \rightarrow 0$ line of ^{12}CO. Since we can easily measure N_{H_2} along any desired line of sight through our simulations, the difficulty comes from the calculation of the integrated intensity. If the gas were optically thin in the $1 \rightarrow 0$ line, then it would be trivial to compute W_{CO}, since the

CO emissivity at any point would depend only on the local values of the temperature, density and chemical abundances and would be effectively decoupled from the conditions elsewhere in the cloud.

Unfortunately, in many of our simulations, some or all of the lines of sight are optically thick in the $1 \rightarrow 0$ line, making it far more challenging to model the CO emission accurately. When the gas is optically thick, it becomes necessary to account for line absorption, which can be ignored in the optically thin case. Furthermore, the opacity and emissivity in the line at any one point in the cloud can couple to the opacity and emissivity at other points in the cloud. Therefore, to model the CO emission entirely accurately, it becomes necessary to calculate the opacities and emissivities for all points in the cloud simultaneously. This is typically accomplished through the use of an iterative method (see e.g. the review of techniques in van Zadelhoff et al. 1992). If the geometry of the gas is relatively simple (e.g. slab symmetry or spherical symmetry), then the resulting problem may still be solved without too much effort. In the present case, however, the density, temperature, chemical composition and velocity structure of the gas are all highly inhomogeneous, and the solution of the coupled equations is a complex and computationally intensive problem that lies outside of the scope of this initial study.

If we are prepared to tolerate a certain amount of uncertainty, however, then it becomes possible to estimate the CO-to-H_2 conversion factor relatively easily, even in optically thick gas. To compute an estimate for the conversion factor, which we denote as $X_{CO,est}$ to distinguish it from the true conversion factor X_{CO}, we use the following procedure. We begin by selecting a set of independent lines of sight through our simulation results. We choose lines of sight that run parallel to the x-axis, one per resolution element. This choice is arbitrary; a different orientation would yield similar results. We then compute H_2 and CO column densities along each of these lines of sight. We next convert each of the CO column densities into an optical depth, τ_{10}, which represents an estimate of the optical depth of the gas in the CO $J = 1 \rightarrow 0$ transition. To perform this conversion, we make three major simplifying assumptions. We assume that all of the CO is in local thermodynamic equilibrium (LTE) and that the gas is isothermal, with a temperature equal to the weighted mean temperature of the gas, where we use the CO number density as an appropriate weighting function

$$T_{mean} = \frac{\sum_{i,j,k} T(i,j,k) n_{CO}(i,j,k)}{\sum_{i,j,k} n_{CO}(i,j,k)}. \tag{11}$$

We also assume that the CO linewidth Δv is uniform and is given by $\Delta v = 3 \text{ km s}^{-1}$. Our choice for Δv is motivated by the fact that our simulations have an rms turbulent velocity of 5 km s^{-1} and that we would expect the one-dimensional velocity dispersion to be a factor of $\sqrt{3}$ smaller than this, i.e. $\sigma_{1D} = 5/\sqrt{3} \simeq 3 \text{ km s}^{-1}$. Given these assumptions, the relationship between N_{CO} and τ_{10} becomes (Tielens 2005)

$$\tau_{10} = \frac{A_{10} c^3}{8\pi v_{10}^3} \frac{g_1}{g_0} f_0 \left[1 - \exp\left(\frac{-E_{10}}{kT}\right) \right] \frac{N_{CO}}{\Delta v}, \tag{12}$$

where A_{10} is the spontaneous radiative transition rate for the $J = 1 \rightarrow 0$ transition, v_{10} is the frequency of the transition, $E_{10} = h v_{10}$ is the corresponding energy, g_0 and g_1 are the statistical weights of the $J = 0$ and $J = 1$ levels, respectively, and f_0 is the fractional level population of the $J = 0$ level. We take values for A_{10} and v_{10} from the Leiden Atomic and Molecular data base (Schöier et al. 2005). In the case that $T_{mean} = 10 \text{K}$, a typical temperature in the highly molecular gas in our simulations, this procedure yields $\tau_{10} \simeq 5 \times 10^{-17} N_{CO}$; i.e. in this case, a CO column density

of approximately $2 \times 10^{16} \text{ cm}^{-2}$ corresponds to an optical depth $\tau_{10} = 1$.

To convert from τ_{10} to W_{CO}, we use the same procedure as in the curve of growth analysis presented in Pineda et al. (2008). We write the integrated intensity as

$$W_{CO} = T_b \Delta v \int_0^{\tau_{10}} 2\beta(\tilde{\tau}) \, d\tilde{\tau}, \tag{13}$$

where T_b is the brightness temperature of the line, Δv is the linewidth and β is the photon escape probability. We approximate β by assuming that it is the same as for a plane-parallel, uniform slab (Tielens 2005):

$$\beta(\tau) = \begin{cases} [1 - \exp(-2.34\tau)]/4.68\tau & \tau \leq 7, \\ \left(4\tau \left[\ln\left(\tau/\sqrt{\pi}\right)\right]^{1/2}\right)^{-1} & \tau > 7. \end{cases} \tag{14}$$

Finally, since we have previously assumed that the CO is in LTE, we simply set $T_b = T_{mean}$.

Using equations (13) and (14), we can compute the integrated intensity for each of our lines of sight. Since we already know the H_2 column density along each line of sight, we could in principle associate a CO-to-H_2 conversion factor with each one. However, as the size of each individual zone in one of our simulations is much smaller than the spatial resolution of observations of all but the few closest GMCs, we feel that it leads to a more meaningful value for $X_{CO,est}$ if we average over the whole cloud, since this is essentially what the limited resolution of the observations forces us to do observationally.

We therefore average over all lines of sight to compute a mean intensity $\langle W_{CO} \rangle$ for the data cube as a whole. Similarly, we compute a mean H_2 column density for the data cube, $\langle N_{H_2} \rangle$, by averaging over all lines of sight. Our estimate of the CO-to-H_2 conversion factor is then simply the ratio of these two quantities:

$$X_{CO,est} = \frac{\langle N_{H_2} \rangle}{\langle W_{CO} \rangle}. \tag{15}$$

Using this procedure, we have computed this estimated CO-to-H_2 conversion factor for each of our simulations and have plotted the resulting values against $\langle A_V \rangle$ in Figs 9 and 10. In Fig. 9, we show the results from all of our runs with non-zero UV backgrounds. In Fig. 10, we compare our results from the runs with no UV with those from the corresponding runs with UV. The canonical value of X_{CO} for the Milky Way, $X_{CO} = 2 \times 10^{20} \text{cm}^{-2} \text{ K}^{-1} \text{ km}^{-1} \text{ s}$ (Dame et al. 2001), is indicated in both figures by a horizontal dashed line.

The first point to note from Fig. 9 is that for our solar metallicity runs with $\langle A_V \rangle > 3$ or, in other words, for simulations with parameters that are a reasonable match to the properties of local GMCs, we find remarkably good agreement between our estimated conversion factor and the measured value. This level of agreement is probably fortuitous to some degree, given the uncertainty in the observational value and the larger uncertainties in our estimated values. Nevertheless, it does indicate that despite our simplifications, our estimates do seem to be successfully capturing the basic physics and are probably trustworthy to within a factor of a few.

A second important point to note from Fig. 9 is that for any given $\langle A_V \rangle$, the CO-to-H_2 conversion factor shows little dependence on metallicity – changes to Z of an order of magnitude or more alter $X_{CO,est}$ by at most a factor of a few. It is therefore not true to say that X_{CO} has a strong dependence on metallicity. Instead, Fig. 9 demonstrates that the true dependence is on the mean extinction $\langle A_V \rangle$. For $\langle A_V \rangle \gtrsim 3$, there is no clear correlation between $X_{CO,est}$ and $\langle A_V \rangle$, but at $\langle A_V \rangle \lesssim 3$, we see a strong correlation. The dependence
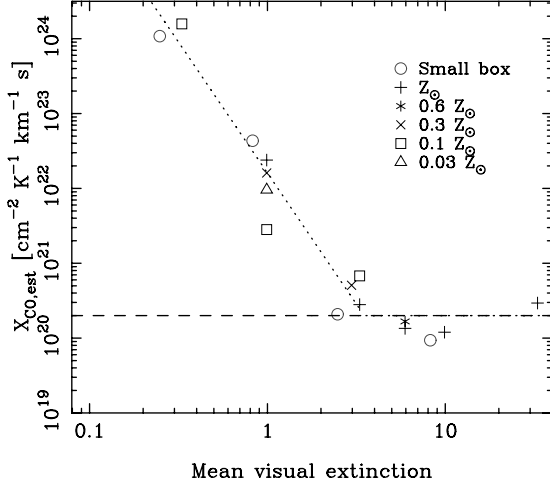
Figure 9. Estimate of the CO-to-H₂ conversion factor $X_{CO,est}$, plotted as a function of the mean visual extinction of the gas, $\langle A_V \rangle$. The simplifications made in our modelling mean that each value of $X_{CO,est}$ is uncertain by at least a factor of 2. At $\langle A_V \rangle > 3$, the values we find are consistent with the value of $X_{CO} = 2 \times 10^{20}$ cm⁻² K⁻¹ km⁻¹ s determined observationally for the Milky Way by Dame et al. (2001), indicated in the plot by the horizontal dashed line. At $\langle A_V \rangle < 3$, we find evidence for a strong dependence of $X_{CO,est}$ on $\langle A_V \rangle$. The empirical fit given by equation (16) is indicated as the dotted line in the figure and demonstrates that at low $\langle A_V \rangle$, the CO-to-H₂ conversion factor increases roughly as $X_{CO,est} \propto A_V^{-3.5}$. It should also be noted that at any particular $\langle A_V \rangle$, the dependence of $X_{CO,est}$ on metallicity is relatively small. Previous claims of a strong metallicity dependence likely reflect the fact that there is a strong dependence on the mean extinction, which varies as $\langle A_V \rangle \propto Z$ given fixed mean cloud density and cloud size.

of $X_{CO,est}$ on $\langle A_V \rangle$ can be described with the following, wholly empirical fitting function, indicated in Fig. 9 by the dotted line:

$$X_{CO,est} \simeq \begin{cases} 2.0 \times 10^{20} & A_V > 3.5, \\ 2.0 \times 10^{20} \, (A_V/3.5)^{-3.5} & A_V < 3.5, \end{cases} \quad (16)$$

where $X_{CO,est}$ has its standard units of cm⁻² K⁻¹ km⁻¹ s. This empirical fitting function is accurate to within a factor of a few over the whole range of $\langle A_V \rangle$ and $X_{CO,est}$ considered in the figure.

Of course, if we consider clouds with a fixed density and size, and merely vary the metallicity, then the strong dependence of $X_{CO,est}$ on the mean extinction implies a strong metallicity dependence, since $\langle A_V \rangle$ is proportional to metallicity. On the other hand, if we vary the metallicity but also allow the mean density or the size of the cloud to vary to compensate, then we will find little or no metallicity dependence.

Fig. 10 demonstrates the importance of UV photodissociation for producing the Galactic CO-to-H₂ conversion factor. In the absence of UV photodissociation, we get comparable values of $X_{CO,est}$ for our $\langle A_V \rangle \simeq 10$ and 30 runs, as one would expect, given that most of the gas in these runs is well shielded from whatever UV is present, but we find significantly smaller values for $X_{CO,est}$ at lower mean extinctions.

It is also of interest to plot the mean values of W_{CO} for the various runs, as this gives a good indication of which of our simulations would correspond to CO-bright clouds, from which it would be easy to detect CO emission, and which would produce CO-faint clouds that would be difficult or impossible to detect in CO. In Fig. 11, we therefore plot $\langle W_{CO} \rangle$ against $\langle A_V \rangle$ for each of our simulations. Given that the noise level for observations of CO in Local Group galaxies is typically of the order of 1 K km s⁻¹ (e.g. Rosolowsky
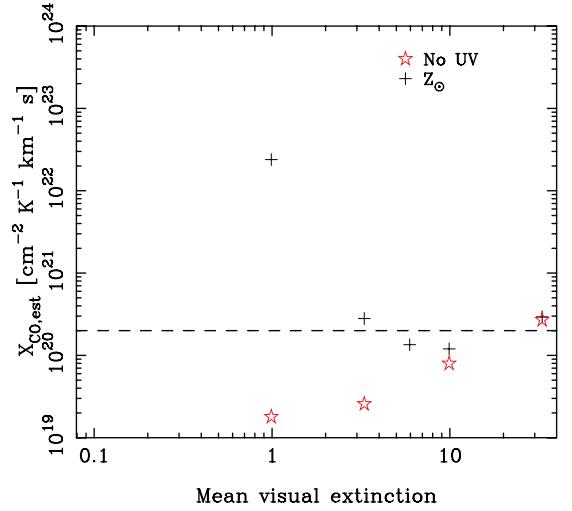

Figure 10. Estimate of the CO-to-H₂ conversion factor $X_{CO,est}$, plotted as a function of the mean visual extinction of the gas, $\langle A_V \rangle$. In this figure, we compare the values obtained for our solar metallicity runs with and without the presence of a UV background. At high $\langle A_V \rangle$, the presence of a UV background has little effect on our derived value of $X_{CO,est}$, but at low $\langle A_V \rangle$, CO photodissociation plays an important role in producing the observed Milky Way value of $X_{CO} = 2 \times 10^{20}$ cm⁻² K⁻¹ km⁻¹ s (Dame et al. 2001), indicated here by the horizontal dashed line.

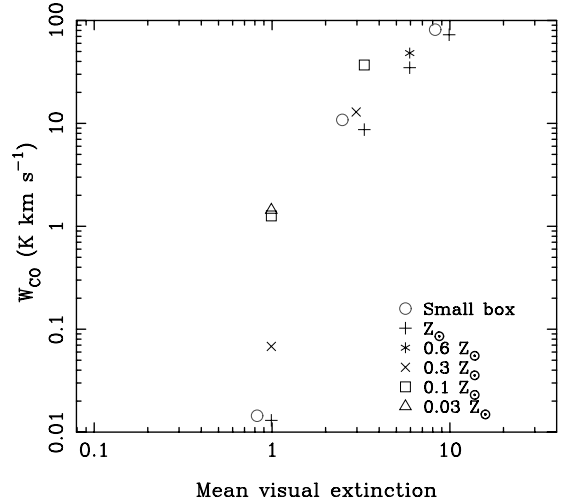**Figure 11.** Velocity-integrated intensity of the $J = 1 \rightarrow 0$ transition in ¹²CO, plotted as a function of the mean extinction of the gas. The symbols are the same as in our previous plots. Noise levels for extragalactic CO observations are typically of the order of 1 K km s⁻¹, so only the runs in the top right-hand quadrant of the plot produce enough CO to be readily detectable.

2007), it is clear that only the runs with $\langle A_V \rangle \gtrsim 1$ will produce CO-bright clouds; runs with lower $\langle A_V \rangle$ will produce clouds that would be extremely difficult to detect with CO observations. Moreover, of the runs with $\langle A_V \rangle \sim 1$, only runs n1000-Z003 and n300-Z01 produce detectable CO: the higher metallicity, lower density runs with $\langle A_V \rangle \sim 1$ yield CO-integrated intensities that would be undetectable.

Finally, it is interesting to speculate how our results for X_{CO} would be affected if we were to consider stronger UV field strengths. In clouds with a high mean extinction, we would not expect the increased UV to have much effect. In these runs, most of the CO is

situated in gas that is already well shielded from the UV background, and even relatively large changes in the strength of the background will not lead to CO photodissociation becoming important in these regions. On the other hand, in runs with low mean extinction, which have most of their CO in gas that is not particularly well shielded from the UV background, a change in the strength of the background will have a much stronger effect. We would therefore expect the values we obtain for X_{CO} in the $\langle A_V \rangle \gtrsim 3$ runs to have little sensitivity to the UV background field strength, and the values we obtain in the $\langle A_V \rangle \lesssim 3$ runs to increase significantly with increasing UV field strength, leading to a steepening of the relationship between X_{CO} and $\langle A_V \rangle$. We plan to test this prediction in future work.

4 DISCUSSION

We can draw a number of immediate conclusions from the results that we have presented in the previous section. First, it seems plain that when we talk about the formation of a molecular cloud, we should draw a distinction between the formation of a cloud in which the hydrogen is primarily in a molecular form and the formation of a cloud from which CO emission can readily be detected, since the conditions for the former are not the same as those for the latter.

To form an H_2-dominated cloud, the cloud must have a mean visual extinction of a few tenths of a magnitude [cf. Krumholz et al. (2008), who find a critical value of approximately 0.5 for a spherical molecular cloud]. More importantly, however, the cloud must survive for long enough to convert most of its atomic hydrogen into H_2. The time required is a strong function of $n_0 Z$, the product of the mean density of the cloud and its metallicity, although the dependence is not linear, and the time required also depends upon the strength and nature of the turbulence (Glover & Mac Low 2007b; Milosavljevic et al., in preparation).

On the other hand, to make a CO-bright cloud, we need a significantly higher mean extinction, $\langle A_V \rangle \gtrsim 3$, but do not require so much time, since the CO abundance in most of the gas comes into equilibrium within 1–2 Myr. In practice, given plausible cloud sizes, clouds that have a high enough mean extinction to be CO-bright will also be dense enough to form H_2 relatively quickly, but the converse is not necessarily true.

Secondly, the existence of a visual extinction threshold above which clouds become CO-bright provides a simple explanation for the observation that in low metallicity systems cloud masses derived from CO observations are significantly smaller than those derived from techniques that do not depend on CO, such as infrared emission (e.g. Israel 1997; Leroy et al. 2007, 2009). In these systems, the CO largely traces the regions of a cloud (or cloud complex) that have mean extinctions greater than 2, but does not trace the H_2 in the surrounding envelope, which may be considerably more extensive and may contain a large fraction of the total mass of the cloud.

Thirdly, the fact that the CO fraction typically reaches equilibrium on a time-scale comparable to or shorter than the crossing time of the cloud and significantly shorter than the time required to assemble the cloud from warm atomic gas implies that CO emission will 'switch on' rapidly during the assembly of the cloud, as hypothesized by Hartmann, Ballesteros-Paredes & Bergin (2001). In the time it takes compressive flows or gravity to double or triple the mean extinction of a cloud with $\langle A_V \rangle \sim 1$, its CO content and luminosity can increase more than a hundredfold. The cloud will therefore quickly move from being effectively unobservable in CO to being readily observable.

On the other hand, the long H_2 formation time-scale implies that molecular clouds need not have equilibrium H_2 abundances, even

once they become CO-bright, contrary to what is often assumed (see e.g. Krumholz et al. 2008; McKee & Krumholz 2010). How far from equilibrium the H_2 fractions are will depend on the cloud properties (mean density, metallicity, rms turbulent velocity, etc.), on the age of the cloud and also on the range of densities considered within the cloud, since overdense regions will reach equilibrium much faster than underdense regions.

Fourthly, we would expect the molecular clouds (or regions thereof) in low metallicity systems that we observe to be CO-bright to also be systematically larger and/or denser than their counterparts in the Milky Way. This conclusion follows from the fact that if $\langle A_V \rangle \gtrsim 3$ is required for CO to form, and we decrease Z, then we must increase either n_0 or L to compensate, since $\langle A_V \rangle \propto n_0 L Z$. This conclusion also lends itself to a relatively simple observational test. If we observe a GMC of size L in a low metallicity system (where L is the total size of the cloud, not of the CO-bright region), and compare it with a cloud of a similar size in the Milky Way, then the former should be systematically denser than the latter. This systematic difference in density may be detectable by examination of the CO(2–1)/CO(1–0) or CO(3–2)/CO(1–0) line ratios, or the ratio of HCN emission to CO emission, all of which will be larger in denser systems.

Finally, our results also suggest a relatively simple explanation for the fact that GMCs observed in the Milky Way span only a small range in column densities (Blitz et al. 2007). The requirement that $\langle A_V \rangle \gtrsim 3$ for a CO-bright cloud implies that any cloud identified as a GMC must have a minimum mean column density of around $60 \, M_\odot \, pc^{-2}$, since clouds with lower column densities will typically not contain much CO.

The distribution of the mean column densities of GMCs above this minimum value depends upon the distributions of the size and mean density of the clouds. However, the cloud size distribution is typically found to be a sharply decreasing function of cloud size L. For example, Heyer, Carpenter & Snell (2001) found $n(L) dL \propto L^{-3.2 \pm 0.1} dL$ for GMCs in the outer Galaxy. If the mean density of the GMCs spans only a small range of values, then the distribution of column densities $n(\Sigma) d\Sigma$ will be a sharply decreasing function of Σ. If we combine this fact with the existence of a minimum column density threshold for a CO-bright GMC, then it implies that most observed GMCs will have column densities that are close to the threshold.

This argument relies on the mean cloud density not being a strong function of the size of the cloud. It is possible to show that this is a good assumption for at least the Heyer et al. (2001) cloud sample. Given a cloud size distribution $n(L) \propto L^{-3.2 \pm 0.1}$, and a constant cloud mean density, then the cloud mass distribution is simply

$$
\begin{aligned}
n(M) \, dM &= n(L) \frac{dL}{dM} dM, \\
&\propto L^{-3.2 \pm 0.1} L^{-2} \\
&\propto M^{-(5.2 \pm 0.1)/3} \\
&\propto M^{-1.73 \pm 0.03},
\end{aligned}
\tag{17}
$$

where we have only assumed that $M \propto L^3$, consistent with our adoption of a constant cloud mean density. For comparison, the cloud mass distribution inferred by Heyer et al. (2001) for this sample of clouds was $n(M) \propto M^{-1.8 \pm 0.03}$, demonstrating that even if the mean density of the clouds is not constant, it can at most be a very weak function of cloud size L.

If this argument is correct, it suggests that most Galactic GMCs should have column densities close to $60 \, M_\odot \, pc^{-2}$. This value is a factor of 3 smaller than the value of $170 \, M_\odot \, pc^{-2}$ determined by

Solomon et al. (1987) that is often taken to be canonical, but is in good agreement with the value recently derived by Heyer et al. (2009) from their re-examination of the Solomon et al. clouds using new data from the Boston University-Five Colleges Radio Astronomy Observatory (FCRAO) Galactic Ring Survey.

We note in conclusion that this argument makes no assumptions about the dynamical equilibrium of the clouds. This casts doubt on the frequently made assumption that the small scatter in observed GMC column densities implies that the GMCs are in virial equilibrium.

5 CAVEATS

There are several caveats that should be borne in mind when considering our results. In our simulations, we use a simplified chemical network for modelling the formation of H_2 and CO and adopt an approximate treatment of the effects of the UV background radiation field. When modelling the CO-integrated intensity, W_{CO}, we make additional approximations, such as the assumption that all of the CO is in LTE or that the CO linewidth has a fixed value. Finally, our simulations neglect the effects of self-gravity, which is clearly important in real molecular clouds.

However, we are confident that these issues will not significantly affect our major results. In Paper I, we showed that our simplified chemical model produces results that agree excellently with the standard UMIST astrochemical model (Le Teuff; Millar & Markwick 2000) over a wide range of parameter space, provided that H, He, C and O are the only elements considered. Including other elements in the chemical model, such as sulphur, will worsen the agreement slightly, particularly in regions dominated by C and C^+, but is unlikely to result in large changes in either the mean abundance of CO or the CO-integrated intensity.

Our simplified treatment of the effects of UV photodissociation will also introduce some error into our predicted CO abundances. Because the dense gas in a molecular cloud has a relatively small volume-filling factor, we can be reasonably confident that our six-ray treatment of the radiation field will tend to overestimate its strength, as it will be more likely to miss shielding coming from dense regions that do not lie on lines of sight parallel to the coordinate axes, than to overestimate the effectiveness of the shielding provided by dense regions that do lie along these lines of sight. However, the main contribution to the photodissociation rate in any particular zone will come from the lines of sight with the lowest column densities. Therefore, if the lines of sight that run parallel to the coordinate axes have low column densities, the fact that we miss the shielding from a few dense regions that do not lie along these lines of sight will not substantially alter the predicted photodissociation rates.

The approximations that we have made in order to derive W_{CO} are another potential source of error. Observationally, we know that not all of the CO in molecular clouds is in LTE (Goldsmith et al. 2008), and so our assumption that it is will cause us to overestimate the integrated intensity. Our assumption that all of the CO has the same temperature is another source of error, although we have attempted to mitigate this by adopting a suitably weighted mean temperature for the gas that gives rise to the CO emission. Our adoption of a fixed linewidth for the CO is also unrealistic; in reality, CO in lower metallicity or lower density systems will be distributed more intermittently and so can be expected to have a lower velocity dispersion than the gas as a whole. However, none of these sources of error will result in a large change in W_{CO}, and moreover they will offset each other to some degree.

Finally, our neglect of the effects of self-gravity is important if one is concerned with the structure of the cloud on the scales of individual dense clumps (e.g. Klessen 2001; Kainulainen et al. 2009). However, the quantities that we have been dealing with in this paper are the results of averaging over the whole cloud, and changes in the cloud structure on scales of a few tenths of a parsec are unlikely to significantly affect these cloud-averaged values. Nevertheless, this is an issue that we intend to return to in the future.

6 SUMMARY

We finish our discussion here by summarizing the key results of this paper. We have shown that the H_2 abundance in turbulent molecular clouds is controlled primarily by the time taken to form the H_2 and that it is relatively insensitive to the effects of UV photodissociation. Photodissociation becomes significant for determining the H_2 abundance only below a visual extinction threshold of a few tenths of a magnitude, in good agreement with previous observational and theoretical work. On the other hand, CO forms rapidly, but is strongly affected by photodissociation. The mean CO abundance falls off rapidly with decreasing mean extinction, particularly in clouds with $\langle A_V \rangle \lesssim 3$.

We have demonstrated that the CO-to-H_2 conversion factor is also determined primarily by the mean extinction of the cloud and that it is almost constant for $\langle A_V \rangle \gtrsim 3$, but falls off as $X_{CO} \propto A_V^{-3.5}$ for $\langle A_V \rangle \lesssim 3$. Furthermore, only the clouds with visual extinctions greater than a few have sufficiently large CO integrated intensities to be detected by current observations. This therefore suggests a simple explanation for the discrepancy observed in low metallicity systems between cloud masses determined by CO observations and those determined by non-CO tracers, such as infrared emission. CO observations inevitably select CO-bright clouds that have mean extinctions large enough to place them in the regime where X_{CO} is approximately constant and equal to the Galactic value. On the other hand, observations that do not rely on CO have no such bias and so select clouds that lie on the power-law portion of the relationship. Therefore, CO observations find an X_{CO} that does not vary significantly with metallicity, while other observations find a strong dependence on metallicity.

Finally, we have shown that if we combine the requirement that $\langle A_V \rangle \gtrsim 3$ for a CO-bright cloud with the observational fact that the GMC size distribution is a steeply decreasing function of size, then we are quite naturally led to the prediction that all GMCs should have near-constant column densities. Therefore, contrary to what is often assumed, the small scatter in observed GMC column densities does not necessarily imply that the GMCs are in virial equilibrium.

REFERENCES

Blitz L., Fukui Y., Kawamura A., Leroy A., Mizuno N., Rosolowsky E., 2007, in Reipurth B., Jewitt D., Keil K., eds, Protostars and Planets V. Univ. Arizona Press, Tucson, AZ, p. 81
Bolatto A. D., Leroy A. K., Rosolowsky E., Walter F., Blitz L., 2008, ApJ, 686, 948
Burton M. G., Hollenbach D. J., Tielens A. G. G. M., 1990, ApJ, 365, 620
Dame T. M., Hartmann D., Thaddeus P., 2001, ApJ, 547, 792
Dickman R. L., 1978, ApJS, 37, 407
Draine B. T., 1978, ApJS, 36, 595
Draine B. T., Bertoldi F., 1996, ApJ, 468, 269
Falgarone E., Phillips T. G., 1996, ApJ, 472, 191
Federrath C., Roman-Duval J., Klessen R. S., Schmidt W., Mac Low M.-M., 2010, A&A, 512, A81
Glover S. C. O., Mac Low M.-M., 2007a, ApJS, 169, 239
Glover S. C. O., Mac Low M.-M., 2007b, ApJ, 659, 1317
Glover S. C. O., Federrath C., Mac Low M.-M., Klessen R. S., 2010, MNRAS, 404, 2 (Paper I)
Godard B., Falgarone E., Pineau des Fôrets G., 2009, A&A, 495, 847
Goldsmith P. F., Heyer M., Narayanan G., Snell R., Li D., Brunt C., 2008, ApJ, 680, 428
Gould R. J., Salpeter E. E., 1963, ApJ, 138, 393
Hartmann L., Ballesteros-Paredes J., Bergin E. A., 2001, ApJ, 562, 852
Hayes J. C., Norman M. L., Fiedler R. A., Bordner J. O., Li P. S., Clark S. E., ud-Doula A., Mac Low M. M., 2006, ApJS, 165, 188
Heiles C., Troland T. H., 2005, ApJ, 624, 773
Heyer M. H., Carpenter J. M., Snell R. L., 2001, ApJ, 551, 852
Heyer M., Krawczyk C., Duval J., Jackson J. M., 2009, ApJ, 699, 1092
Hollenbach D., McKee C. F., 1979, ApJS, 41, 555
Israel F. P., 1997, A&A, 328, 471
Joulain K., Falgarone E., Pineau des Fôrets G., Flower D., 1998, A&A, 340, 241
Kainulainen J., Beuther H., Henning T., Plume R., 2009, A&A, 508, L35
Klessen R. S., 2001, ApJ, 556, 837
Kramer C., Jakob H., Mookerjea B., Schneider N., Brüll M., Stutzki J., 2004, A&A, 424, 887
Kritsuk A. G., Norman M. L., Padoan P., Wagner R., 2007, ApJ, 665, 416
Krumholz M. R., McKee C. F., Tumlinson J., 2008, ApJ, 689, 865

Le Petit F., Nehmé C., Le Bourlot J., Roueff E., 2006, ApJS, 164, 506
Le Teuff Y. H., Millar T. J., Markwick A. J., 2000, A&AS, 146, 157
Lee H.-H., Herbst E., Pineau des Forêts G., Roueff E., Le Bourlot J., 1996, A&A, 311, 690
Leroy A., Bolatto A., Stanimirovic S., Mizuno N., Israel F., Bot C., 2007, ApJ, 658, 1027
Leroy A. K. et al., 2008, ApJ, 702, 352
Lesaffre P., Gerin M., Hennebelle P., 2007, A&A, 469, 949
Mac Low M.-M., 1999, ApJ, 524, 169
Mac Low M.-M., Klessen R. S., 2004, Rev. Modern Phys., 76, 125
Mac Low M.-M., Klessen R. S., Burkert A., Smith M. D., 1998, Phys. Rev. Lett., 80, 2754
McKee C. F., Krumholz M. R., 2010, ApJ, 709, 308
Maloney P., Black J. H., 1988, ApJ, 325, 389
Meixner M., Tielens A. G. G. M., 1993, ApJ, 405, 216
Mookerjea B., Kramer C., Röllig M., Masur M., 2006, A&A, 456, 235
Norman M. L., 2000, Rev. Mex. Astron. Astrofis., 9, 66
Padoan P., Nordlund Å., Jones B. J. T., 1997, MNRAS, 288, 145
Pineda J. E., Caselli P., Goodman A. A., 2008, ApJ, 679, 481
Röllig M. et al., 2007, A&A, 467, 187
Rosolowsky E., 2007, ApJ, 654, 240
Rosolowsky E., Engargiola G., Plambeck R., Blitz L., 2003, ApJ, 599, 258
Rubio M., Boulanger F., Rantakyro F., Contursi A., 2004, A&A, 425, 1
Sanders D. B., Solomon P. M., Scoville N. Z., 1984, ApJ, 276, 182
Savage B. D., Bohlin R. C., Drake J. F., Budich W., 1977, ApJ, 216, 291
Schmidt W., Federrath C., Hupp M., Kern S., Niemeyer J. C., 2009, A&A, 494, 127
Schöier F. L., van der Tak F. F. S., van Dishoeck E. F., Black J. H., 2005, A&A, 432, 369
Sembach K. R., Howk J. C., Ryans R. S. I., Keenan F. P., 2000, ApJ, 528, 310
Solomon P. M., Rivolo A. R., Barrett J., Yahil A., 1987, ApJ, 319, 730
Spaans M., van Dishoeck E. F., 1997, A&A, 323, 953
Sternberg A., Dalgarno A., 1995, ApJS, 99, 565
Stoerzer H., Stutzki J., Sternberg A., 1996, A&A, 310, 592
Strong A. W., Mattox J. R., 1996, A&A, 308, L21
Tielens A. G. G. M., 2005, The Physics and Chemistry of the Interstellar Medium. Cambridge Univ. Press, Cambridge
van Zadelhoff G.-J. et al., 1992, A&A, 395, 373
Wilson C. D., 1995, ApJ, 448, L97

This paper has been typeset from a T$_{\rm E}$X/L$^{\rm A}$T$_{\rm E}$X file prepared by the author.